Regulating electrocatalytic properties of oxygen reduction reaction via strong coupling effects between Co-NC sites and intermetallic Pt₃Co

Weiping Xiao [a,b,*], Daqiang Yan [a], Qin Zhao [a], Danil Bukhvalov [a], Xiaofei Yang [a,**]

[a] *College of Science, Institute of Materials Physics and Chemistry, Nanjing Forestry University, Nanjing 210037, China*
[b] *Key Laboratory of Advanced Energy Materials Chemistry (Ministry of Education), College of Chemistry, Nankai University, Tianjin 300071, China*

ARTICLE INFO

ABSTRACT

Developing the Pt-based intermetallic nanoparticles could accelerate the sluggish kinetic of oxygen reduction reaction, while it remains a great challenge to explore efficient synthesis strategies enhancing thermal stabilities and electrocatalytic properties. This work employed the metal-support coupling strategy to construct the Pt₃Co/CoNC hierarchical nanostructure, where the well-dispersed atomically ordered Pt₃Co nanoparticles were anchored on the Co-NC sites. Physical structure analysis combined with density functional theory calculations demonstrated the strong coupling effect between Pt and surrounding Co-NC sites, which could weaken the activation energy to break O-O bonds and enhance the intrinsic activity and stability of Pt. Hence, the Pt₃Co/CoNC exhibited the optimized ORR activities with the half-wave potentials of 0.97 V in KOH solution and displayed the peak power density of 187 mW cm^{-2} as the cathode of Zn-air battery. This metal-support coupling strategy can be further generalized and improved to synthesize other Pt-based catalysts with efficient electrocatalytic properties.

1. Introduction

To enhance the energy conversion efficiency of Fuel cells and Zn-air batteries, it is crucial to develop cost-effective, high-efficiency, and durable electrocatalysts that facilitate the sluggish oxygen reduction reaction (ORR) [1–4]. While precious metal platinum (Pt) has demonstrated excellent catalytic performance, its scarcity and high cost limit large-scale practical applications [5,6]. Alloying Pt with 3d transition metals (M: Fe, Ni, and Co) to formation Pt$_x$M alloy catalysts could reduce the loading of Pt as well as the cost of the catalyst to some extent [7–10]. Furthermore, introducing transition metals with a small atomic radius into Pt could result in the strain and alloy effects, which may weaken the adsorption energy of intermediate reactants in the ORR and facilitate to the enhancement of intrinsic ORR performance [11]. Compared with disordered PtM alloys, the atomically structure ordered intermetallic have been reported to enhance the intrinsic activity and stability originated from the strong 3d-5d orbital interaction between M and Pt [12–14]. However, achieving ordered structures typically requires high temperatures (> 700 °C), involving energy input to overcome the rearrangement of Pt and M atoms [15]. The PtM nanoparticles at this

temperature are always prone to agglomeration, inevitably causing a reduction in Pt utilization and electrochemical active areas. Therefore, it is of great significance to explore a suitable dispersion carrier, aiming to avoid agglomeration of Pt alloy during the formation of intermetallic structure.

Metal-organic frameworks (MOFs) consist of transition metal and organic ligands, which have regular polyhedral structure and can be evolved to porous crystalline materials (M-N-C) maintaining the dimensional stability to some extent [16–19]. The obtained M-N-C can provide more internal space and act as the active sites to facilitate the ORR kinetics, while it is hindered by the insufficient stability especially in acidic solution. However, the active M-N-C are equipped with enough defects and pores that can anchor Pt atoms and prevent its aggregation [20]. This distinguishes them from conventional supports that only provide surface interactions. More importantly, the introduced Pt atoms could combine with the transition metals (Fe/Co/Zn) in M-N-C and transform into PtM alloy phase after high-temperature annealing [21]. These alloy nanoparticles dispersed on the carbon supports with high porosity and excellent stability in catalytic reactions. Utilizing the synergistic effect between Pt and MOFs-derived metal/carbon materials can

---

* Corresponding author at: College of Science, Institute of Materials Physics and Chemistry, Nanjing Forestry University, Nanjing 210037, China.
** Corresponding author.
E-mail addresses: wpxiao@njfu.edu.cn (W. Xiao), xiaofei.yang@njfu.edu.cn (X. Yang).

not only improve the atomic utilization of Pt but also enhance the catalytic performance [22]. For instance, matrices derived from Co-containing and Zn-containing zeolitic imidazolate frameworks (ZIFs) can combine with Pt to form PtZn [23] and Pt_xCo [24], respectively, which showed excellent ORR activities and stabilities. Nevertheless, few efforts have been devoted to exploring the electronic metal-support interaction between M-N-C and Pt-based intermetallic compound, enhancing the catalytic performance and improving the utilization of Pt. Based on the above analysis, M-N-C features hierarchical pore structure, high surface area, and abundant heterogeneous dopants, providing additional benefits to strengthen metal-support interaction and regulate the electronic structure for possible enhancements of intrinsic activity and thermal stability of Pt-based alloy. Nevertheless, few efforts have been devoted to exploring the metal-support interaction between M-N-C and Pt-based intermetallic compound, enhancing the catalytic performance as well as improving the utilization of Pt. Furthermore, it is still challenge to develop an innovative strategy to in-situ anchoring intermetallic Pt-based nanoparticles by M-N-C, revealing the catalytic mechanism and elucidating the synergistic interaction.

Herein, the synergistic strategy was employed to enhance the intrinsic activities of Pt sites by integrating the atomically ordered Pt_3Co with Co-NC sites. The Co-NC with polyhedron structure was derived from Zn/Co-ZIF under high temperature annealing process, which could anchor the precursor of Pt and provide Co atom to formation the atomically ordered $Pt_3Co/CoNC$ by control annealing temperature. The abundant pore structure and sites of Co-NC effectively prevent the aggregation of Pt alloys and enable the uniformly distribution of Pt_3Co nanoparticles. The $Pt_3Co/CoNC$ catalyst showed excellent ORR catalytic activity with half-wave potential of 0.96 V and 0.97 V in $HClO_4$ and KOH solutions. $Pt_3Co/CoNC$ also exhibited excellent stabilities with the half-wave potential increased 4 mV after 30,000 cycles in 0.1 mol L^{-1} $HClO_4$. Density functional theory (DFT) calculations and XPS analysis elucidated that the reallocation of electrons between Co-NC and Pt atoms weakened the adsorption energy of oxygen-containing species, facilitating the breakage of O-O bonds and enhancing the intrinsic ORR activity of $Pt_3Co/CoNC$. Furthermore, $Pt_3Co/CoNC$, as the air electrode in Zn-air battery, displayed the peak power density of 187 mW cm^{-2} and discharge potential of 1.25 V at the current densities of 5 mA cm^{-2}. This scheme provides a feasible and effective strategy to enhance the ORR intrinsic activities of Pt-based intermetallic structure by the coupling effects of Co-NC sites.

2. Experimental section

2.1. Materials preparations

Cobalt nitrate hexahydrate ($Co(NO_3)_2 \cdot 6H_2O$, AR, 99%), Zinc nitrate hexahydrate ($Zn(NO_3)_2 \cdot 6 H_2O$, AR, 99%), 2-methylimidazole (AR, 99%) and Chloroplatinic acid hexahydrate ($H_2PtCl_6 \cdot 6 H_2O$, AR, 37.5%) were obtained from Shanghai Aladdin Biochemical Technology Co. Ltd. Perchloric acid ($HClO_4$, 72.0 wt%) was purchased from Nanjing Chemical Reagent Co., Ltd. Methyl Alcohol (CH_3OH, 99.9%) was acquired from Anhui Tiandi High Purity Solvent Co. Ltd. Ethanol (C_2H_5OH, 99%) was purchased from Sinopharm Group Chemical Reagent Co., Ltd. All of the chemicals in this experiment were analytical grade and used without further purification.

2.2. Synthesis of ZIF-67, ZIF-8 and Zn/Co-ZIF

Firstly, 2-methylimidazole (1.50 g) was dissolved in 15 mL of methanol and swiftly added to a methanol solution (35 mL) containing $Co(NO_3)_2 \cdot 6 H_2O$ (2.76 g) with continuous stirring. The resulting mixture was allowed to stand at room temperature for 24 h. Subsequently, the obtained product was washed with methanol and separated through centrifugal, which was dried in vacuum oven at 60 °C to obtain purple product, named as ZIF-67. The synthesis method of ZIF-8 was roughly

same to that of ZIF-67, except that $Zn(NO_3)_2 \cdot 6 H_2O$ (2.79 g) was used in place of $Co(NO_3)_2 \cdot 6 H_2O$ (2.76 g), and the reaction product was white. The solution with 2-methylimidazole (3.08 g) and methanol (35 mL) was added into the mixed solution with $Co(NO_3)_2 \cdot 6 H_2O$ (2.76 g), Zn $(NO_3)_2 \cdot 6 H_2O$ (2.79 g) and methanol (75 mL) to prepare Zn/Co-ZIF.

2.3. Synthesis of Co/C, Zn/C and $ZnCo_2O_4/C$

ZIF-67, ZIF-8 and Zn/Co-ZIF were annealed under flowing N_2 atmosphere at 700 °C for 3 h to achieve ideal carbonization of the precursors and obtain black products, which were named as Co/C, Zn/C and $ZnCo_2O_4/C$, respectively.

2.4. Synthesis of PtCo/CoNC、PtZn/ZnNC and $Pt_3Co/CoNC$

Taking the synthesis of PtCo/CoNC as an example. On the basis of the mass ratio of Pt to Co/C is 1:4, 40 mg of the Co/C sample and 2.0 mL of chloroplatinic acid solution (ρPt: 5.0 mg mL^{-1}) were added into the round-necked flask and stirred for 8 h at constant temperature of 70 °C. The obtained precipitate was washed with ethanol and collected by centrifuge. Subsequently, the collected material was dried in a vacuum oven. Finally, this product was annealed at 300 °C for 1 h and then at 700 °C for 1 h in H_2/Ar (5/95) atmosphere to obtain black sample, named as PtCo/CoNC. The specific operation steps of PtZn/ZnNC and $Pt_3Co/CoNC$ were the same as those of PtCo/CoNC. PtZn/ZnNC and $Pt_3Co/CoNC$ were obtained from Zn/C and $ZnCo_2O_4/C$ loaded with Pt and then annealing treated at high temperature, respectively.

2.5. Characterization of catalysts

The morphology of catalysts was surveyed by scanning electron microscope (SEM, JSM-7600 F, Japan); Microscopic topography and elemental mapping of the sample were obtained at transmission electron microscopy (TEM, JEM-1400, Japan). X-ray photoelectron spectroscopy (XPS, AXIS UltraDLD, Japan) was utilized to investigate chemical elements and valence states of C, O, N, Pt elements. The crystallographic information was confirmed by the multifunctional horizontal X-ray diffractometer (XRD, Ultima IV, Japan); Raman spectrometer (Raman, DXR-532, USA) was employed to evidence the carbon structure. The mass percent of Pt was detected from the inductively coupled plasma (ICP-OES 730) measurements.

2.6. Electrochemical measurements of catalysts

All electrochemical measurements were performed via the three-electrode system (CHI 760E, Shanghai Chenhua, China). The graphite rod and reversible hydrogen electrode (RHE) were served as the counter electrode and reference electrode, respectively. The working electrodes were prepared by spreading catalyst ink onto rotating disk electrode (RDE, glass carbon area: 0.196 cm^{-2}). For the catalyst ink, 2.0 mg catalyst was dispersed onto 0.2 mL Nafion/isopropyl alcohol (1‰) solution. Then, 10 μL catalyst ink was dropped on the pre-cleaned RDE surface and dried naturally, the mass loading of Pt was about 102 μg cm^{-2}. The cyclic voltammetry (CV) curves of the catalysts were recorded at a scan rate of 50 mV s^{-1} within a potential range of 0.05–1.0 V (vs. RHE) in a N_2-saturated solution. ORR polarization curves were obtained within a potential range of 0.2–1.1 V vs. RHE at a scan rate of 5 mV s^{-1}, following 90% iR correction and rotating speeds of 1600 rpm in an O_2-saturated solution. The evaluation of ORR stability involved continuously conducting 30,000 CV cycles from 0.6 V to 1.0 V at the scanning speed of 100 mV s^{-1} in 0.1 M $HClO_4$. After every 10,000 CV cycles, LSV test was conducted with fresh electrolyte to assess the degree of decay and stability of the catalyst. The electrochemically active surface areas (ECSAs) were calculated based on CO striping curves in 0.1 mol L^{-1} $HClO_4$ solution.

$$ECSA = Q/0.42 \quad (1)$$

Q is the integrated charge in the CO desorption region, and 0.42 is the electricity required for Pt to adsorb a single layer of CO per unit area (mC cm^{-2}).

The specific activities were calculated by normalizing the kinetic current by the ECSA. Mass activities were calculated based on the actual Pt content in the sample, measured by inductively coupled plasma (ICP). The electron transfer numbers of the catalysts were calculated according to the Koutecky-Levich (K-L) equation.

$$\frac{1}{J} = \frac{1}{J_k} + \frac{1}{J_L} = \frac{1}{J_k} + \frac{1}{B\omega^{1/2}} \quad (2)$$

$$B = 0.62nFC_0(D_0)^{2/3}\upsilon^{-1/6} \quad (3)$$

Where j is the measured current density; J_K and J_L represent kinetic and diffusion-limited current densities, respectively; ω represents the angular velocity of the disk; F is Faraday constant (96485 C mol^{-1}); C_0 is the volume concentration of O_2 (1. achieving ordered structures typically requires high temperatures ($> 700\,°C$), involving energy input to overcome the rearrangement of Pt and M atoms$\times 10^{-3}$ mol L^{-1}); D_0 is the diffusion coefficient of O_2 in electrolyte (1.9×10^{-5} cm^2 s^{-1}); υ is the kinematic viscosity of the electrolyte (1.09×10^{-2} cm^2 s^{-1}).

The calculation formula of mass activity (MA) is as follows:

$$MA = \frac{J_m}{Pt(wt)} \quad (4)$$

2.7. Computational Methods

Theoretical modelling was carried out using SIESTA pseudopotential code [25], employing the generalised gradient approximation (GGA-PBE) [26] for the exchange-correlation potential in a spin-polarised mode. A full optimisation of the atomic positions was carried out, during which the electronic ground state was consistently found using norm-conserving pseudopotentials [27] for the cores, with a double-ξ-plus polarisation basis for the localised orbitals of non-hydrogen atoms and a double-ξ for hydrogen atoms. The forces and total energies were optimised with an accuracy of 0.04 eV Å^{-1} and 1.0 meV/cell (or less than 0.02 meV/atom), respectively.

2.8. Zn-air batteries tests

The performances of Zn-air batteries were tested in a homemade cell composed with polished Zn foil, air cathode and electrolyte. The air cathode was prepared by dispersing catalyst ink on carbon cloth with catalyst loading of 0.8 mg cm^{-2} and dried naturally. The electrolyte contained 0.2 M zinc acetate and 6 M KOH. LSV discharging curves were carried out on the CHI 760E electrochemical station. The rate performance and long-term discharge performance was tested on the CT3002A LAND.

3. Results and discussion

The atomically ordered Pt$_3$Co/CoNC catalyst was synthesized by using liquid-phase assembling and high-temperature annealing process as shown in Fig. 1. Briefly, Zn^{2+} and Co^{2+} with a certain proportion were integrated with 2-methylimidazole by self-assembly reaction to obtain Zn/Co-ZIF, which has uniform polyhedral structure and contains Zn-N and Co-N bonds. The effective carbonization of Zn/Co-ZIF was realized under N$_2$ atmosphere after annealing treated at 700 °C, resulting in that the organic ligands in the precursor were converted into carbon matrix with excellent electrical conductivity. Meanwhile, the Zn^{x+} was partially removed under aeration conditions, and the remaining Zn^{x+} and Co^{x+} were converted to metal oxides forming ZnCo$_2$O$_4$/C. The obtained ZnCo$_2$O$_4$/C could anchor Pt^{x+} through electrostatic adsorption, and the mixture were annealed at high temperature under Ar/H$_2$ to prepare Pt$_3$Co/CoNC series catalysts. Moreover, the Zn^{2+} and Co^{2+} could be independently coordinated with 2-methylimidazole to form ZIF-8 and ZIF-67, which was further composited with Pt forming PtZn/ZnNC and PtCo/CoNC, respectively.

Fig. 2 showed the morphologies of different precursors and their composites at various annealing stages. The ZIF-8 precursor exhibited a regular polyhedral morphology with an approximate size of 1000–1200 nm as shown in Fig. 2a. After the first annealing treatment under N$_2$ atmosphere, the obtained Zn/C showed almost no polyhedral morphology since the instability of Zn in high-temperature ($> 400\,°C$, Fig. 2b). Compositing the Zn/C and Pt could gain the PtZn/ZnNC through secondary heat treatment, which is no longer possessed the same polyhedral structure as the ZIF-8 precursor (Fig. 2c). The ZIF-67 also exhibited polyhedral morphology with unified size of 500–600 nm and smooth surface, which is much smaller than that of ZIF-8 (Fig. 2d). After the first annealing treatment, the Co/C showed a less regular polyhedral structure with rough surface grown many small protuberances like carbon nanotube, which could be originated by the catalytic effect of Co (Fig. 2e). This may be attributed to the fact that the melting point of Co is much higher than Zn, leading to less loss of Co during the annealing process. The Co/C can anchor Pt to prepared PtCo/CoNC at high temperature treatment. The polyhedral structure and carbon nanotubes were damaged in PtCo/CoNC composites, which could be owing to the excessive exfoliation of polyhedral surface components in annealed process (Fig. 2f). Fig. 2g confirmed that Zn/Co-ZIF equipped the same regular polyhedral structure as ZIF-8/ZIF-67 with well-defined size of 600–700 nm. The morphology of ZnCo$_2$O$_4$/C maintained polyhedral structure with smooth surface after the first annealing treatment as shown in Fig. 2h. Furthermore, ZnCo$_2$O$_4$/C loaded with Pt could obtain the Pt$_3$Co/CoNC after the secondary heating treatment at 700 °C. The original morphology of Zn/Co-ZIF retained excellently and formed uniformly distributed porous structure on the surface of Pt$_3$Co/CoNC-700 (Fig. 2i). The Pt$_3$Co/CoNC samples acquired at annealing temperature of 500 and 900 °C, showed discriminately different morphology as shown in Fig. S1. The morphology of the Pt$_3$Co/CoNC-500 samples showed almost no change, while the Pt$_3$Co/CoNC-
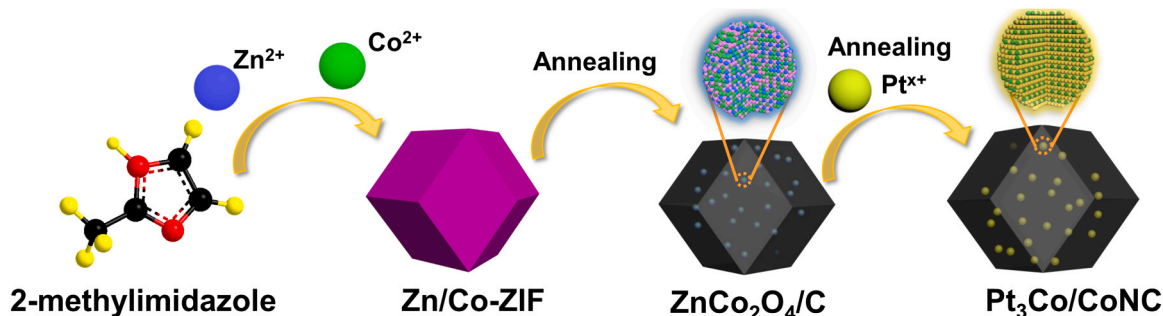

Fig. 1. The synthesis illustration of the Pt$_3$Co/CoNC catalysts.
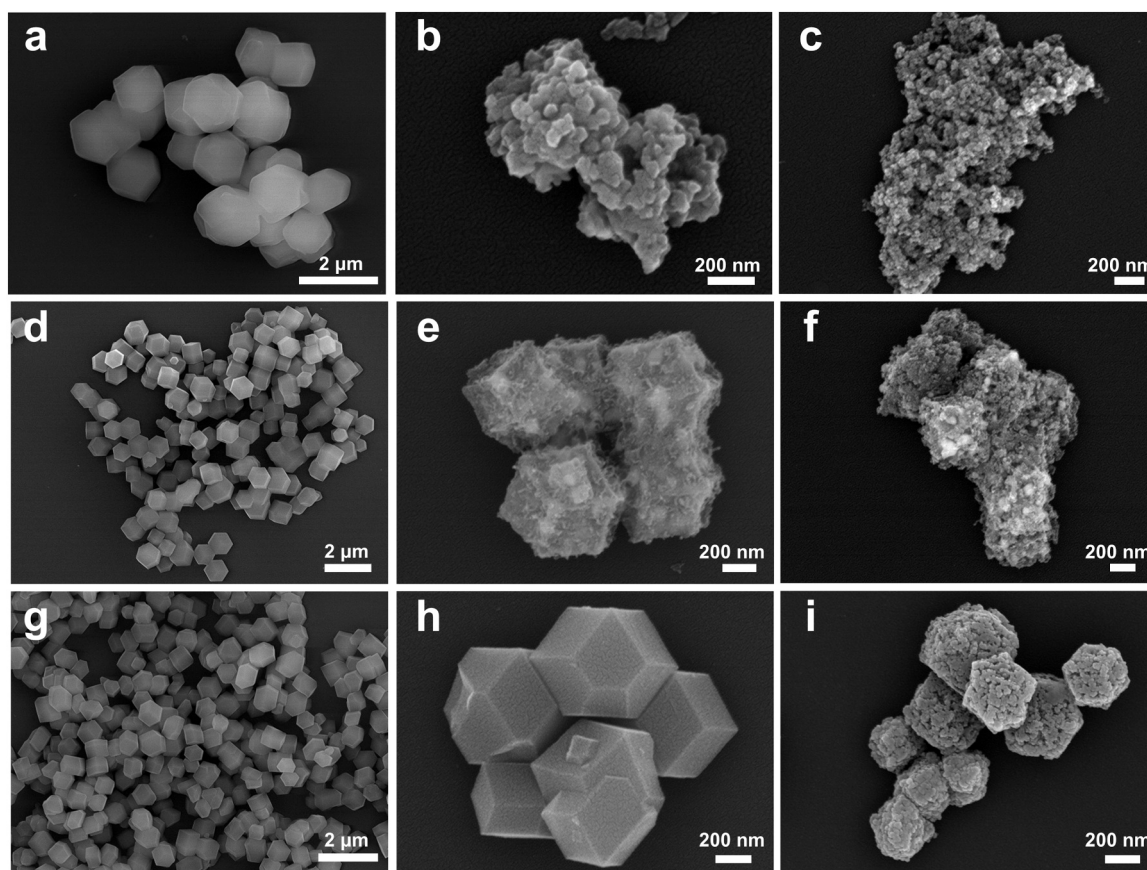
Fig. 2. The SEM images of (a) ZIF-8, (b) Zn/C, (c) PtZn/ZnNC, (d) ZIF-67, (e) Co/C, (f) PtCo/CoNC, (g) Zn/Co-ZIF, (h) ZnCo$_2$O$_4$/C, (i) Pt$_3$Co/CoNC.

900 samples showed the agglomeration of Pt nanoparticles and formed unexpected porous structure.

The TEM images were employed to further analyze the morphology of PtZn/ZnNC, PtCo/CoNC and Pt$_3$Co/CoNC composites. As shown in Fig. 3a, PtZn/ZnNC composites did not retain the dodecahedron shape of ZIF-8, and the larger particles had a size of about 200 nm, indicating significant particle agglomeration after secondary annealing treatment. Meanwhile, the PtCo/CoNC presents the shape of a polyhedron derived from ZIF-67 and the particles are agglomerated obviously with a size of about 50 nm, which is much smaller than that of PtZn, suggesting slight damage to the shape of PtCo/CoNC (Fig. 3b). The Pt$_3$Co/CoNC retained the regular polyhedron morphology originated from Zn/Co-ZIF as shown in Fig. 3c. The nanoparticles are uniformly distributed in the polyhedral framework with a size of about 15 nm, which is much smaller and more uniform than that of PtCo and PtZn. The high magnification TEM images in Fig. S2 also illustrated that the Pt$_3$Co nanoparticles were more regular and uniformly distributed in the carbon matrix relative to that of PtCo and PtZn, indicating bimetal makes carbon substrate more stable. This could be ascribed to that the Zn/Co-ZIF exhibits different porosity, specific surface area, gas adsorption compared with ZIF-8 and ZIF-67 [28,29]. This difference in structure makes them have different thermal stability. To further figure out the detailed structure, high-resolution TEM (HRTEM) images were conducted on the obtained Pt$_3$Co/CoNC, PtCo/CoNC and PtZn/ZnNC samples. Fig. 3d showed the HRTEM image of PtZn/ZnNC and the interplanar spacing was measured to be 0.35 nm, agreeing with supperlattice diffraction peaks of the (001) on ordered PtZn particles. Fig. 3e showed the HRTEM picture of PtCo/CoNC and the clearly visible lattice spacing of 0.37 nm corresponding to the supperlattice (001) crystal plane of ordered PtCo particles. Similarly, the supperlattice diffraction peak crystal plane corresponding to the (100) crystal plane of

Pt$_3$Co was also found in the HRTEM image in Pt$_3$Co/CoNC, and the crystal plane spacing was calculated to be 0.38 nm as shown in Fig. 3f. The existence of crystal planes with supperlattice diffraction peaks indicated that the formation of structurally ordered intermetallic compounds in the above three samples, which also verified the feasibility of the preparation method. From the ICP results, the actual content of Pt in the PtZn/ZnNC,PtCo/CoNC and Pt$_3$Co/CoNC catalysts were 35.8%, 37% and 25%, respectively (Table S1). Fig. 3g-i showed the STEM images and the corresponding elemental mappings of PtZn/ZnNC, PtCo/CoNC, and Pt$_3$Co/CoNC. It can be seen that the nitrogen was presented uniformly on the view of catalysts, indicating an excellent nitrogen doping environment in the carbon matrix. The Pt element was corresponded well to Zn and Co in the bright nanoparticles, while there are also Pt and Zn/Co near the particles, indicating a fractional of Zn/Co or Pt is doped in the carbon matrix in the form of atom. At the same time, the distribution of element mapping images of Pt and Co in Pt$_3$Co/CoNC was the more uniformly than that of PtZn/ZnNC and PtCo/CoNC. This further verifies the good distribution of Pt$_3$Co intermetallic compounds in carbon matrix, which could be attributed to that the introduction of Zn can reduce the grain size of Pt alloy and make it evenly distributed [30].

The XRD patterns were employed to analyze crystal structure and phase composition of the obtained samples. Fig. S3a compared the XRD patterns of Zn/C, Co/C, and ZnCo$_2$O$_4$/C. There was a peak located at almost 25° corresponding to carbon and no appearance of characteristic peaks related to Zn for the Zn/C, indicating the Zn is easily volatilized and less prone to form crystal. The Co/C obtained from ZIF-67 showed three characteristic peaks located at 41.2°, 51.5° and 75.8°, corresponding to the (111), (200) and (220) planes of Co (PDF# 15–0806). For the ZnCo$_2$O$_4$/C sample obtained from Zn/Co-ZIF after heating treatment, the characteristic peaks at 42.4°, 61.5° and 73.7° in the XRD pattern matched with the (200), (220) and (311) crystal planes of CoO
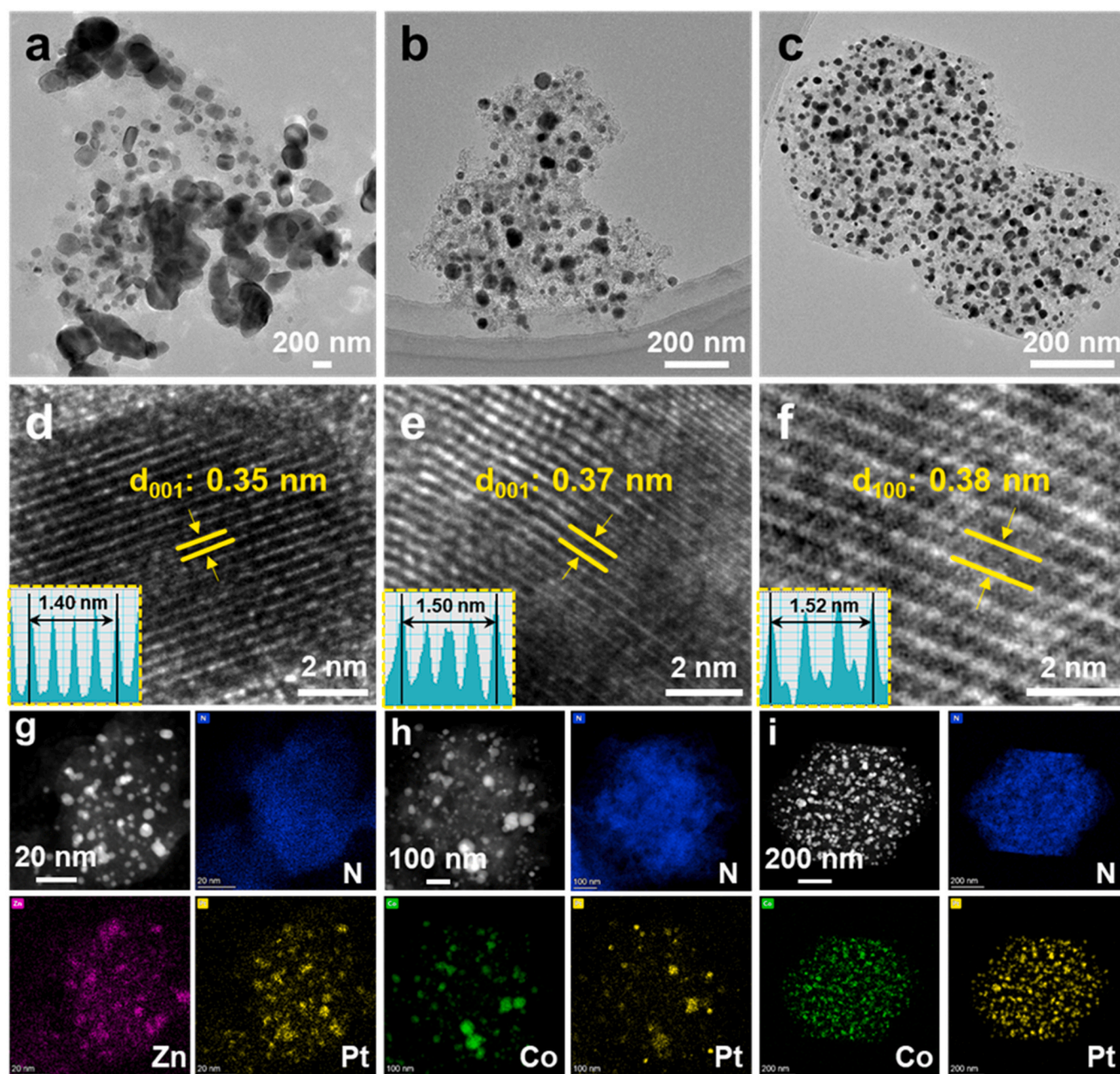
Fig. 3. The TEM images of (a) PtZn/ZnNC, (b) PtCo/CoNC, (c) Pt₃Co/CoNC. The HRTEM image of (d) PtZn/ZnNC, (e) PtCo/CoNC, (f) Pt₃Co/CoNC. The STEM image and the corresponding element mapping image of (g) PtZn/ZnNC, (h) PtCo/CoNC, (i) Pt₃Co/CoNC.

(PDF#43–1004). Furthermore, the characteristic peaks at 18.9°, 31.2°, 36.8°, 59.3° and 65.1° correspond to (111), (220), (311), (511) and (440) planes of $ZnCo_2O_4$ (PDF#23–1390), indicating that Zn and Co in the precursors formed bimetallic oxides during the annealing process. Meanwhile, the content of metallic Co in the annealed samples is higher than that of Zn, which could provide conditions for the preparation of Pt_3Co intermetallic compounds. Fig. 4a shows the XRD characteristic peaks of PtZn/ZnNC, PtCo/CoNC, and Pt₃Co/CoNC samples obtained from the secondary heat treatment of the carbonized ZIFs and Pt precursors in H_2/Ar atmosphere. For the PtZn/ZnNC, the characteristic peaks located at 25.3°, 31.3°, 40.8°, 44.8°, 52.2°, 62.2°, 65.5°, 71.4° and 74.3° are corresponded to the (001), (110), (111), (200), (002), (112), (220), (202) and (310) planes of atomically ordered PtZn (PDF#06–0604). The characteristic peaks located at 24.0°, 33.3°, 41.5°, 47.6°, 49.3°, 54.1°, 60.8°, 69.9° and 71.0° are related to the (001), (110), (111), (200), (002), (201), (112), (220) and (202) planes of atomically

ordered PtCo (PDF#43–1358). The characteristic peaks located at 23.0°, 32.8°, 40.5°, 47.1°, 53.1°, 58.6° and 68.8°, corresponding to the (100), (110), (111), (200), (210), (211) and (220) planes of atomically ordered Pt₃Co (PDF#29–0499). According to the intensity analysis of the XRD peaks, the ordering degree of the Pt₃Co/C is about 66.1% (Table S2). The existence of the diffraction peaks of the superlattice proves the formation of ordered intermetallic compounds for PtZn/ZnNC, PtCo/CoNC, and Pt₃Co/CoNC, which is coordinated with the HRTEM results. In order to study the relationship between annealing temperature and phase composition, the secondary annealed temperature was chosed as 500 °C, 700 °C and 900 °C. The characteristic peaks of the samples annealed at 500 °C showed four peaks attributed to the plane of Pt (PDF#04–0802), while the samples annealed at 700 °C and 900 °C possessed obvious characteristic peaks of atomically ordered Pt₃Co as shown in Fig. S3b. The Raman spectra of PtZn/ZnNC, PtCo/CoNC and Pt₃Co/CoNC showed the existence of carbon-specific G peaks and D peaks, indicating that
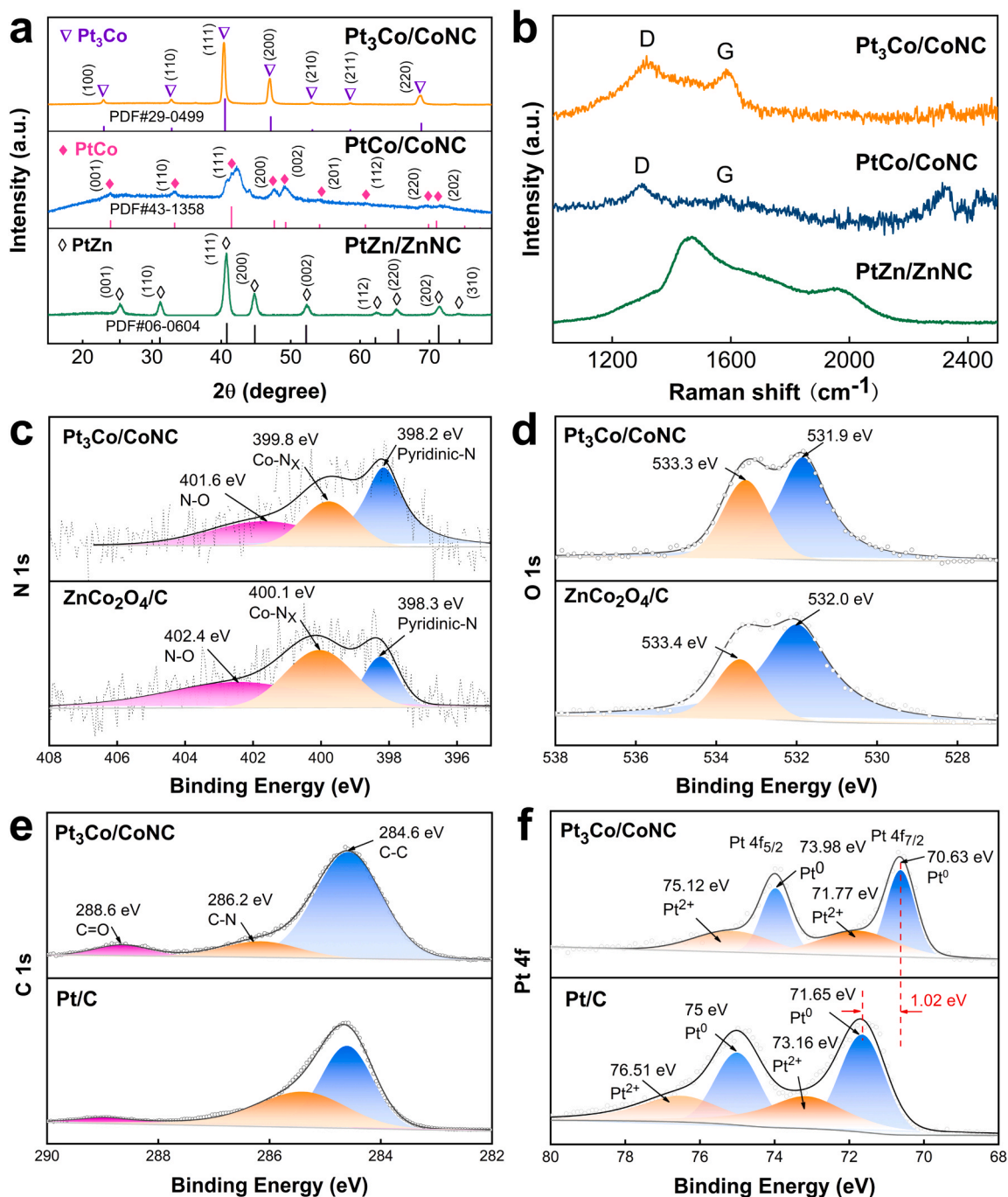
Fig. 4. (a) XRD and (b) Raman patterns of PtZn/ZnNC, PtCo/CoNC, and Pt$_3$Co/CoNC. XPS spectra of (c) N 1 s and (d) O 1 s in ZnCo$_2$O$_4$/C and Pt$_3$Co/CoNC. XPS spectra of (e) C 1 s and (f) Pt 4 f in Pt$_3$Co/CoNC and Pt/C.

high temperature annealing realized the transformation from organic ligands to carbon matrix [31] (Fig. 4b).

The element chemical states of the obtained catalysts were analyzed by using XPS spectrum. Fig. S4 showed the XPS spectra of ZnCo$_2$O$_4$ and Pt$_3$Co/CoNC. It is confirmed the existence of C, N, O and Co elements in ZnCo$_2$O$_4$/C (Fig. S4a). The C, N, O, Co and Pt elements were also found in XPS spectrum of Pt$_3$Co/CoNC (Fig. S4b). The appearance of Pt 4 f verified the successful integration of Pt with ZnCo$_2$O$_4$/C. The XPS spectrum of N 1 s in ZnCo$_2$O$_4$/C can be divided into three peaks located at 398.8 eV, 400.1 eV and 402.4 eV (Fig. 4c), corresponding to pyridine nitrogen, Co-N$_x$ and N-O bond [32]. The corresponding characteristic peaks of pyridine nitrogen, Co-N$_x$ and N-O bond of N 1 s in Pt$_3$Co/CoNC

were located at 398.2 eV, 399.8 eV and 401.6 eV, respectively, which were shifted to the lower binding energy direction compared with the fitted peaks of N 1 s in ZnCo$_2$O$_4$/C. The presence of pyridine nitrogen further indicated that nitrogen-doped metal micro-environment was formed inside the samples, facilitating the adsorption of intermediates and enhancement of ORR performance [33]. Fig. 4d compared the XPS spectra of O 1 s in ZnCo$_2$O$_4$/C and Pt$_3$Co/CoNC. The fitting peaks of O 1 s in Pt$_3$Co/CoNC were located at 531.9 eV and 533.3 eV corresponding to Co-O and H$_2$O, which shifted towards lower binding energy relative to that on ZnCo$_2$O$_4$/C located at 532.0 eV and 533.4 eV [34].

As shown in Fig. 4e, XPS spectrum of C 1 s in Pt$_3$Co/CoNC fitted three characteristic peaks at 284.6 eV, 286.2 eV and 288.6 eV, corresponding

to C-C, C-N and C=O bonds, respectively [35]. This indicated that the N-doped structure was still maintained in $Pt_3Co/CoNC$ samples, which is consistent to the results of element mapping. The high-resolution Pt 4 f XPS spectrum in $Pt_3Co/CoNC$ and Pt/C can be fitted to Pt^0 and Pt^{2+} (Fig. 4f). For $Pt_3Co/CoNC$, the characteristic peaks located at 73.98 eV and 70.63 eV are corresponding to 4 $f_{5/2}$ and 4 $f_{7/2}$ of Pt^0, while the peaks at 75.12 eV and 71.77 eV are corresponding to 4 $f_{5/2}$ and 4 $f_{7/2}$ of Pt^{2+}, respectively. Compared with Pt/C, the binding energy of $Pt_3Co/$-CoNC showed a negative shift of 1.02 eV, investigating the significantly change of internal electronic structure and the enhanced electronegativity of Pt in $Pt_3Co/CoNC$ [36,37].

The ORR catalytic activities of Pt/C, PtZn/ZnNC, PtCo/CoNC, and $Pt_3Co/CoNC$ were evaluated using cyclic voltammetry and linear sweep voltammetry in N_2-saturated 0.1 M $HClO_4$ electrolyte. The CV curves in the potential range of 0.05 V to 0.4 V revealed that the $Pt_3Co/CoNC$ exhibited more obvious adsorption and desorption peaks of hydrogen compared to other catalysts, suggesting higher electrochemically active areas (Fig. S5). Fig. 5a presents the LSV curves of the catalysts for ORR. $Pt_3Co/CoNC$ showed a significantly higher half-wave potential ($E_{1/2}$) of 0.96 V relative to that of Pt/C (0.86 V), PtZn/ZnNC (0.89 V), and PtCo/CoNC (0.93 V). The fitted slopes of the Tafel curves calculated from the ORR polarization curves of $Pt_3Co/CoNC$ was 63 mV dec^{-1}, which is
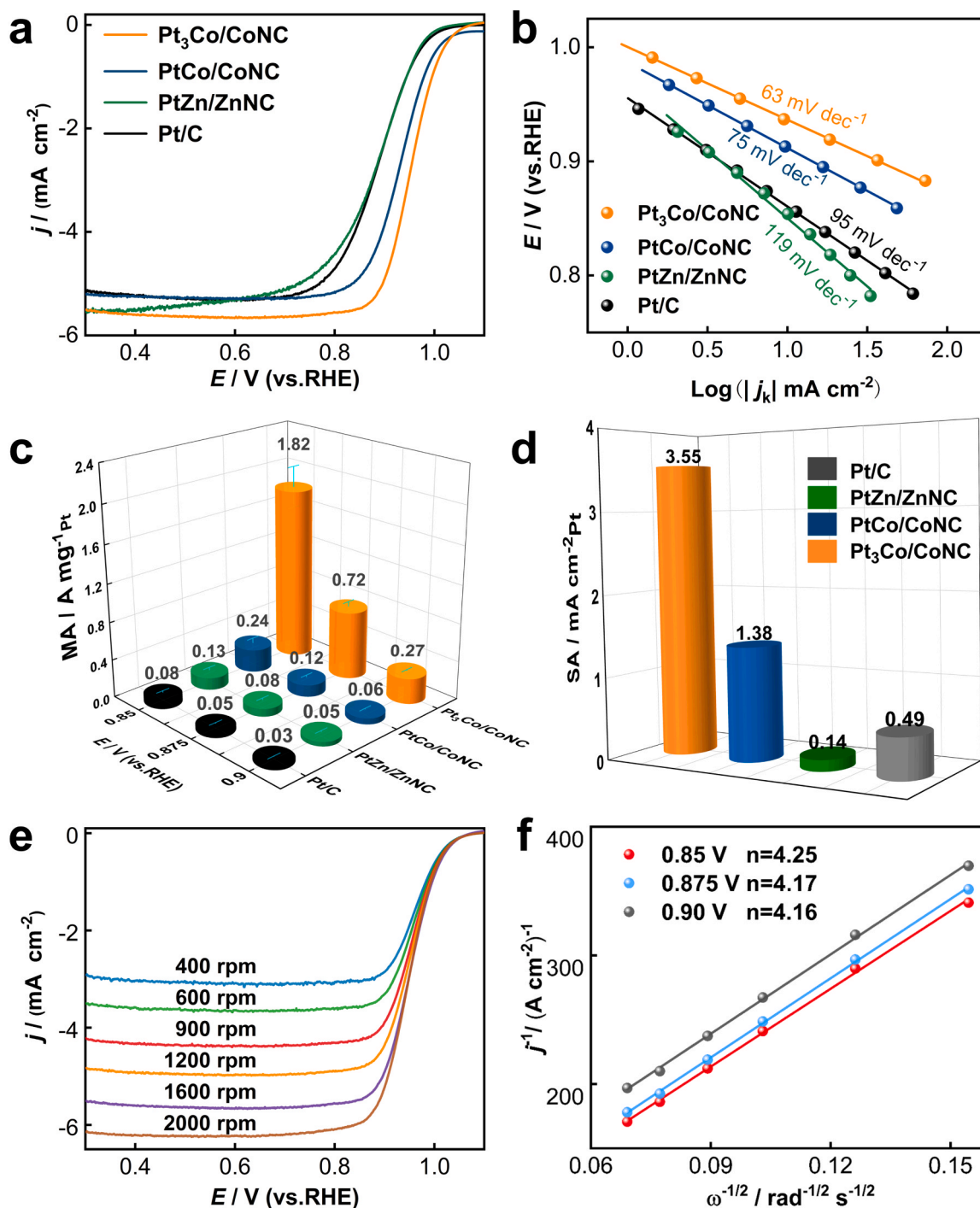

Fig. 5. (a) ORR polarization and (b) the corresponding Tafel curves of Pt/C, PtZn/ZnNC, PtCo/CoNC and $Pt_3Co/CoNC$. (c) Mass activities and (d) specific activity at 0.85 V, 0.875 V, 0.90 V. (e) ORR polarization curves at different rotational speeds and (f) the corresponding K-L plots of $Pt_3Co/CoNC$.

much lower than Pt/C (95 mV dec^{-1}), PtZn/ZnNC (119 mV dec^{-1}) and PtCo/CoNC (75 mV dec^{-1}), suggesting the fast ORR kinetics on Pt$_3$Co/CoNC (Fig. 5b). The mass activity was calculated by normalizing the kinetic current to mass of Pt. The obtained mass activity of Pt$_3$Co/CoNC reached nearly 10 times than that of Pt/C under 0.85 V, 0.875 V and 0.90 V as shown in Fig. 5c, which is comparable to the mass activities of Pt-based oxygen reduction catalysts reported in recent years (Table S3). Furthermore, the electrochemically surface areas (ECSA) could be calculated according to the CO-stripping curves. Fig. S6 showed the CO-stripping curves of Pt/C, PtZn/ZnNC, PtCo/CoNC and Pt$_3$Co/CoNC catalysts. The first cycles of CO-stripping curves showed desorption peak of CO, while the second cycles of CO-stripping curves showed desorption peak of hydrogen, indicating the CO was adsorbed on the surface of catalysts. The ECSA of Pt$_3$Co/CoNC was calculated to be 0.57 m^2 g$_{Pt}^{-1}$, nearly two-times of Pt/C (Fig. S7). The corresponding specific activity of Pt$_3$Co/CoNC were determined to be 3.55 mA cm$_{Pt}^{-2}$ at 0.875 V, which is much higher than that of Pt/C (0.49 mA cm$_{Pt}^{-2}$), PtZn/ZnNC (0.14 mA cm$_{Pt}^{-2}$) and PtCo/CoNC (1.38 mA cm$_{Pt}^{-2}$) (Fig. 5d). To investigate the reaction mechanism of Pt$_3$Co/CoNC, LSV curves under different speeds from 400 to 2000 rpm were performed and the current densities was enhanced with the speed rotation increased (Fig. 5e). The corresponding Koutecky-Levich (K-L) diagram showed nearly parallel fitting lines, indicating that the electron transfer number was basically the same at different potential (Fig. 5f). The average number of transferred electrons (n) at 0.85 V, 0.875 V and 0.90 V obtained from the K-L curves were 4.25, 4.17 and 4.16, respectively, which is further verified four-electron reaction pathway of ORR for Pt$_3$Co/CoNC in 0.1 mol L^{-1} HClO$_4$ solution. Electrochemical performance of different samples was also evaluated in 0.1 M KOH solution. Fig. 6a and Fig. S8 showed the

ORR polarization curves and the half-wave potentials ($E_{1/2}$) of Pt$_3$Co/CoNC is 0.97 V, which is much higher than that of Pt/C (0.85 V), PtZn/ZnNC (0.91 V), PtCo/CoNC (0.95 V) and ZnCo$_2$O$_4$/C (0.87 V). The mass activities of different catalysts at 0.85 V, 0.875 V and 0.90 V were calculated by normalizing the kinetics current to the mass of Pt. The Pt$_3$Co/CoNC displayed a mass activity of 1.67 A mg$_{Pt}^{-1}$ at 0.85 V, which is much higher relative to Pt/C (0.02 A mg$_{Pt}^{-1}$), PtZn/ZnNC (0.11 A mg$_{Pt}^{-1}$) and PtCo/CoNC (1.01 A mg$_{Pt}^{-1}$). At the same time, the mass activity of Pt$_3$Co/CoNC at 0.875 V and 0.9 V were also much higher than the others, verifying that Pt$_3$Co/CoNC was also equipped best ORR catalytic performance in alkaline solution (Fig. 6b). ORR polarization curves of Pt$_3$Co/CoNC measured at different rotational speeds showed that the limiting current densities increased with the rotational speed as shown in Fig. 6c. Noticeably, the number of transferred electrons calculated from the K-L curves of Pt$_3$Co/CoNC were 3.42, 3.50 and 3.40 at 0.85 V, 0.875 V and 0.90 V, respectively, which also verified that a nealy four-electron pathway of ORR in 0.1 M KOH solution (Fig. 6d). The electron transfer number of Pt$_3$Co/CoNC is less than 4, which could be ascribed to the OH$^-$ ions existed in KOH electrolyte [38,39].

The stability of the catalyst determines the actual service life of catalytic benefits. All of catalysts were subjected to 30,000 cycles in the potential range of 0.6–1.0 V in 0.1 M HClO$_4$ electrolyte. The CV curves of Pt/C, PtZn/ZnNC, PtCo/CoNC and Pt$_3$Co/CoNC were significantly reduced compared with the initial curves, while the CV curves of Pt$_3$Co/CoNC showed smaller attenuation after 30,000 cycles of potential cycling (Fig. S9). Compared with the initial data in Pt$_3$Co/CoNC, the area of hydrogen region in the CV curve increased after durability test, which indicates the increase of electrochemical active area and the improvement of performance (Fig. S9d). To further evaluate the stability
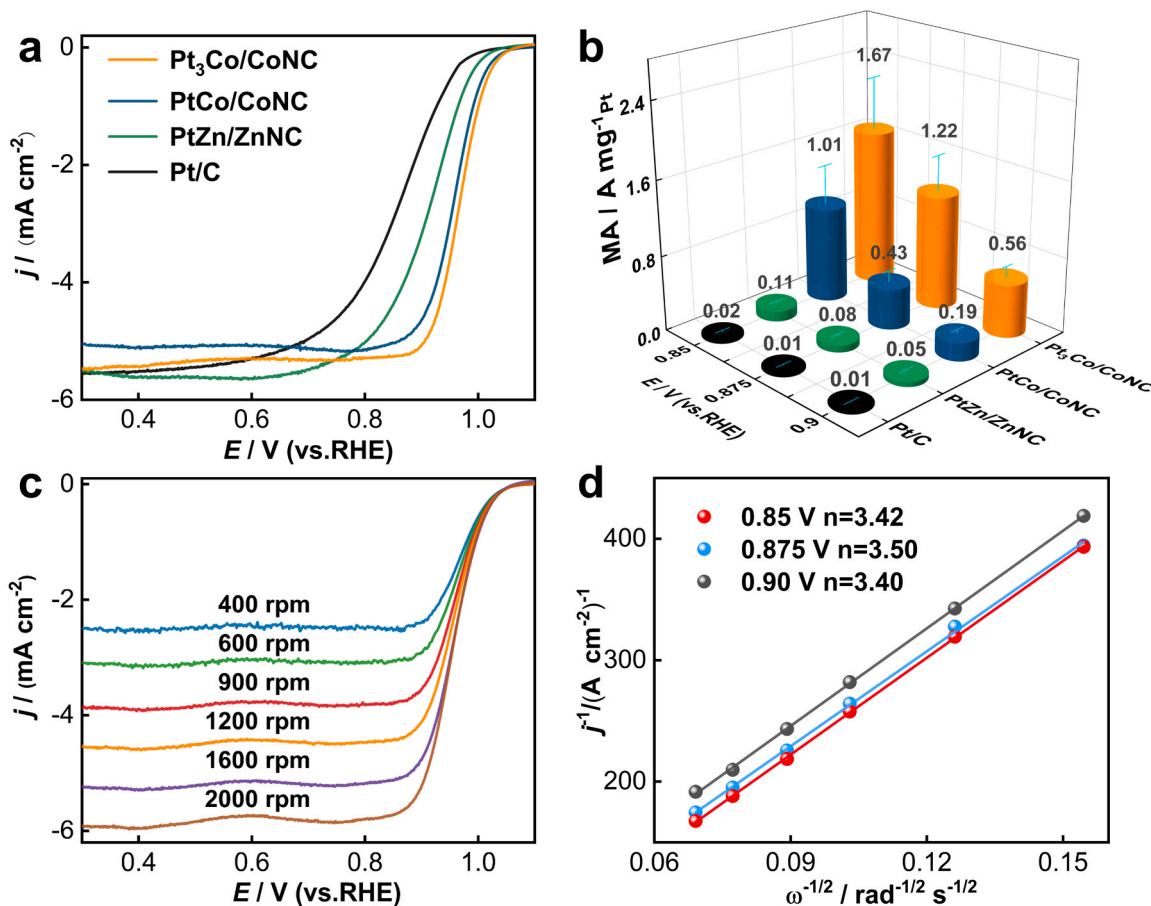

Fig. 6. Electrochemical test results in 0.1 M KOH solution. (a) ORR polarization curves and (b) Mass activities of Pt/C, PtZn/ZnNC, PtCo/CoNC and Pt$_3$Co/CoNC. (c) ORR polarization curves of Pt$_3$Co/CoNC at different rotational speeds and (d) the corresponding K-L curves.

of the catalysts, oxygen reduction reaction polarization curves were tested in the initial state and after 30,000 cycles. The half-wave potential of Pt/C and PtZn/ZnNC were attenuated for 460 mV (Fig. S10) and 130 mV, respectively, while the half-wave potential of PtCo/CoNC decayed only 10 mV after the stability test (Figs. 7a, 7b, 7c). In addition, the half-wave potential of Pt$_3$Co/CoNC was increased 4 mV, which verified the excellent catalytic stability of the Pt$_3$Co intermetallic compound. Fig. 7d exhibited the corresponding mass activities of the catalysts at 0.875 V initial and after 30,000 potential cycles, where the Pt$_3$Co/CoNC showed minimal degree of decay after the stability testing compared with other catalysts. The excellent stability in Pt$_3$Co/CoNC could be ascribed to the synergistic effect of the atomically ordered Pt$_3$Co and N-doped carbon matrix. The TEM images of Pt$_3$Co/CoNC composite materials after stability testing were further analyzed. As shown in Fig. 8a, Pt$_3$Co/CoNC retains its original polyhedral carbon-based profile structure, where the nanometer-sized particles uniformly distributed, which is consistent with the initial morphology (Fig. 3c). The TEM images in Fig. 8b-c reveal the regular distribution of Pt$_3$Co nanoparticles with the size of ~15 nm within the carbon matrix, indicating that the bimetallic nanoparticles remain stable after stability testing. To gain a more detailed understanding of the structure, Fig. 8d-e present HRTEM images of Pt$_3$Co/CoNC. The interplanar spacing was measured to be 0.22 nm and 0.27 nm, corresponding to the (111) and (110) lattice diffraction peaks of ordered Pt$_3$Co. The existence of superlattice diffraction peak of (110) proves that the ordered structure of the intermetallic compound was still maintained after multiple stability tests. Fig. 8f-g displayed the STEM images and the corresponding elemental maps of Pt$_3$Co/CoNC for large areas and single grains. The

distribution of Pt and Co elements corresponds well with the bright nanoparticles, indicating that Pt and Co elements are uniformly distributed in Pt$_3$Co/CoNC. This further confirms the excellent stability of Pt$_3$Co intermetallic compounds within the carbon matrix. Moreover, the distributions of Pt and Co elements in the single particles indicate that the Pt shell was formed on the surface of Pt$_3$Co particles, which was attributed to the dissolution of surface Co during the stability test (Fig. 8g). The formation of Pt shell can prevent the dissolution of internal Co and make the catalyst have better stability, which is the reason why the hydrogen zone area of the CV curve increases and the stability is good after stability test. Furthermore, the XPS was conducted on the Pt$_3$Co/CoNC and compared before and after the stability tests. Fig. 8h showed the high-resolution spectrum of Pt 4 f, in which the characteristic peaks with binding energies located at 71.63 eV and 74.95 eV were corresponding to the Pt 4 f$_{7/2}$ and Pt 4 f$_{5/2}$ orbitals of Pt^0, and the characteristic peaks located at 72.61 eV and 75.87 eV were corresponding to the Pt 4 f$_{7/2}$ and Pt 4 f$_{5/2}$ orbitals of Pt^{2+}. Compared with the pre-stability sample, the binding energies of the peaks were shifted to a higher degree by ~1.0 eV, suggesting that the strong coupling effect between Pt and Co-NC sites effectively enhanced the stability of the samples [40]. Fig. 8i showed the high-resolution spectra of N 1 s before and after the stability test, and the Co-Nx peak area increased significantly after the stability test, confirming the enhanced effect of the Co-Nx site, which is facilitate to the enhancement of catalytic performance.

The density functional theory was employed to evaluate the ORR performance enhancement mechanism, and the reaction steps and methods for the calculation of the free energy of the reactions are
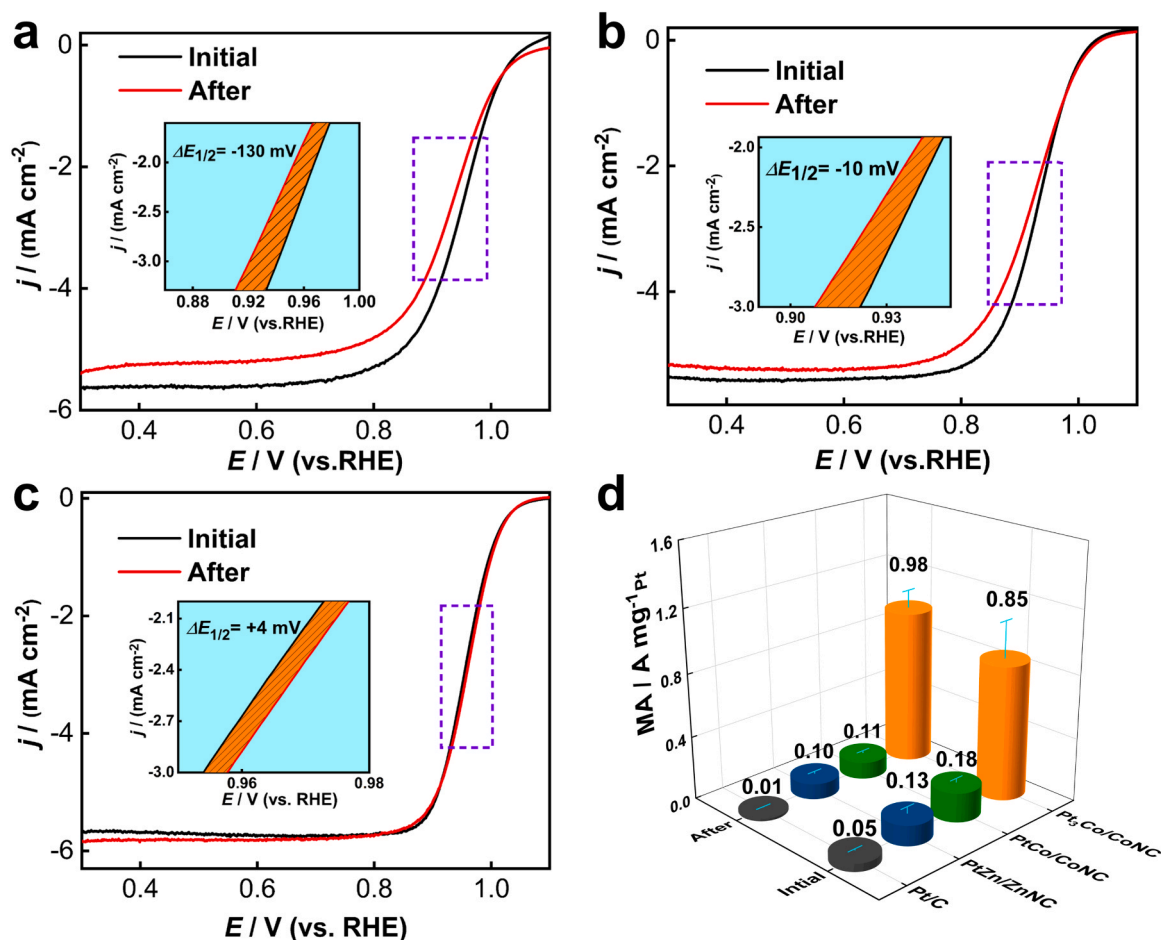

Fig. 7. ORR polarization curves of (a) PtZn/ZnNC, (b) PtCo/CoNC, (c) Pt$_3$Co/CoNC catalysts initial and after 30,000 potential cycles. (d) The mass activities of the catalysts initial and after 30,000 potential cycles.
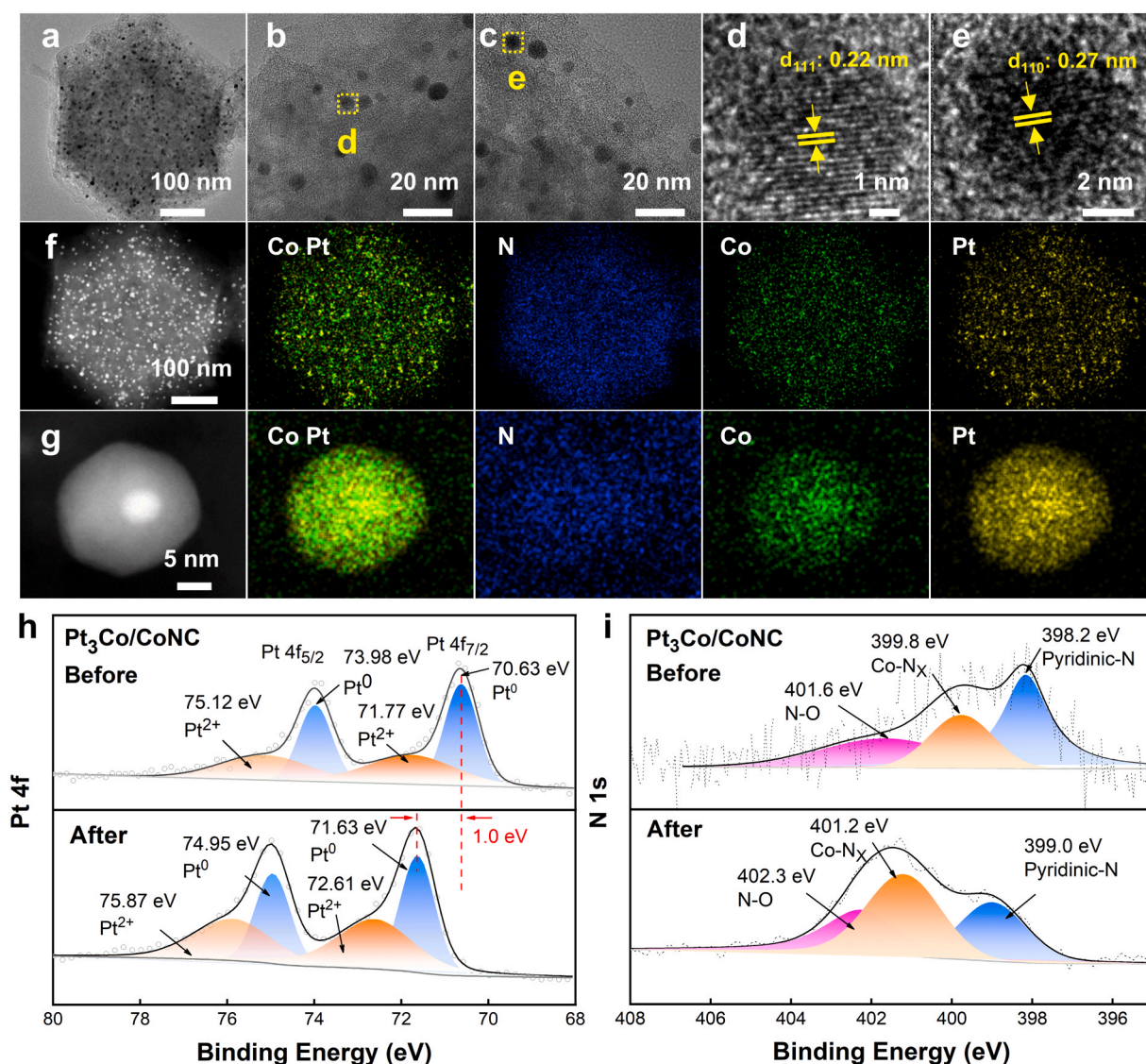
Fig. 8. TEM images of Pt₃Co/CoNC catalyst after 30,000 potential cycles. TEM images in the scale bar of (a) 100 nm and (b, c) 20 nm. (d, e) HRTEM images of the selected region (yellow squares) in b and c. STEM image and elemental mappings of N, Co, Pt for (f) large areas and (g) single grains. XPS spectra of (h) Pt 4 f and (i) N 1 s in Pt₃Co/CoNC before and after stability test.

referred to the reported literature [41–43]. For simplicity, the free energy diagram is drawn only for U = 1.23 eV. For the simulation of the Pt-nanoparticles covered by CoNC centers, we used slab of 8 layers of fcc-Pt with the surface corresponding with [111] crystallographic direction covered by graphene monolayer with single Co atom in surrounding of four nitrogen atoms (Fig. 9a). Note that for (111) surface of fcc-Pt in-lane lattice parameters multiplied by five is almost exactly coincide with lattice parameters of graphene multiplied by six. This fact guided our choice of supercell. We performed calculations for fixed lattice parameters because metallic substrate is rather rigid. Formation of the interface provides charge redistribution along whole interface (Fig. 9b). Because Pt substrate and graphitized carbon distance is rather big (about 0.35 nm), changes of charge density in the areas of graphitized carbon distant from Co-N center is minor. Contrary, significant redistribution of charge densities were observed between Pt substrate and Co-N center. This redistribution of the charge densities corresponds with significant changes in electronic structure of Co-centers (Fig. 9c). In free-standing CoNC membrane, electronic structure of Co demonstrates localization of the electrons on the orbitals similar to oxides. Formation of metallic Co-Pt bonds provides metallization (vanishing of the energy gap) of electronic structure of Co. The source of this metalization is

broadening of the sharp peak near Fermi level corresponding with participation of this localized electron in Co-Pt bond. The cyan cloud under Co-center is corresponding with "donation" of the electron to substrate, and yellow cloud over Pt-surface demonstrate "acceptance" of this electron (Fig. 9b). To check effect of described changes in electronic structure of CoNC, we performed simulation of ORR over CoNC, Pt (111) and Pt/CoNC. Because there is only one metallic center in CoNC substrate, four electron ORR process was considered and the results of the calculations were shown on Fig. 9d. The better catalytic performance is corresponding with the magnitudes of the free energies closer to zero. Results of our calculations demonstrates that catalytic properties of CoNC systems is superior over Pt (Fig. 9d). But the presence of Pt-substrates slightly improves catalytic performance of CoNC systems. Additionally, discussing above changes of the electronic structure on Co-center and in vicinity, mechanical stabilization of CoNC membrane by formation of multiple substrate-cover non-covalent bonds could also slightly improve catalytic properties of CoNC monolayer.

Utilizing the rechargeable liquid ZABs to evaluate the practical application of Pt₃Co/CoNC as shown in Fig. 10a. The Pt/C (20 wt%) was tested for comparison. The Discharge polarization curves of the Pt₃Co/CoNC and Pt/C were displayed in Fig. 10b. The discharge current
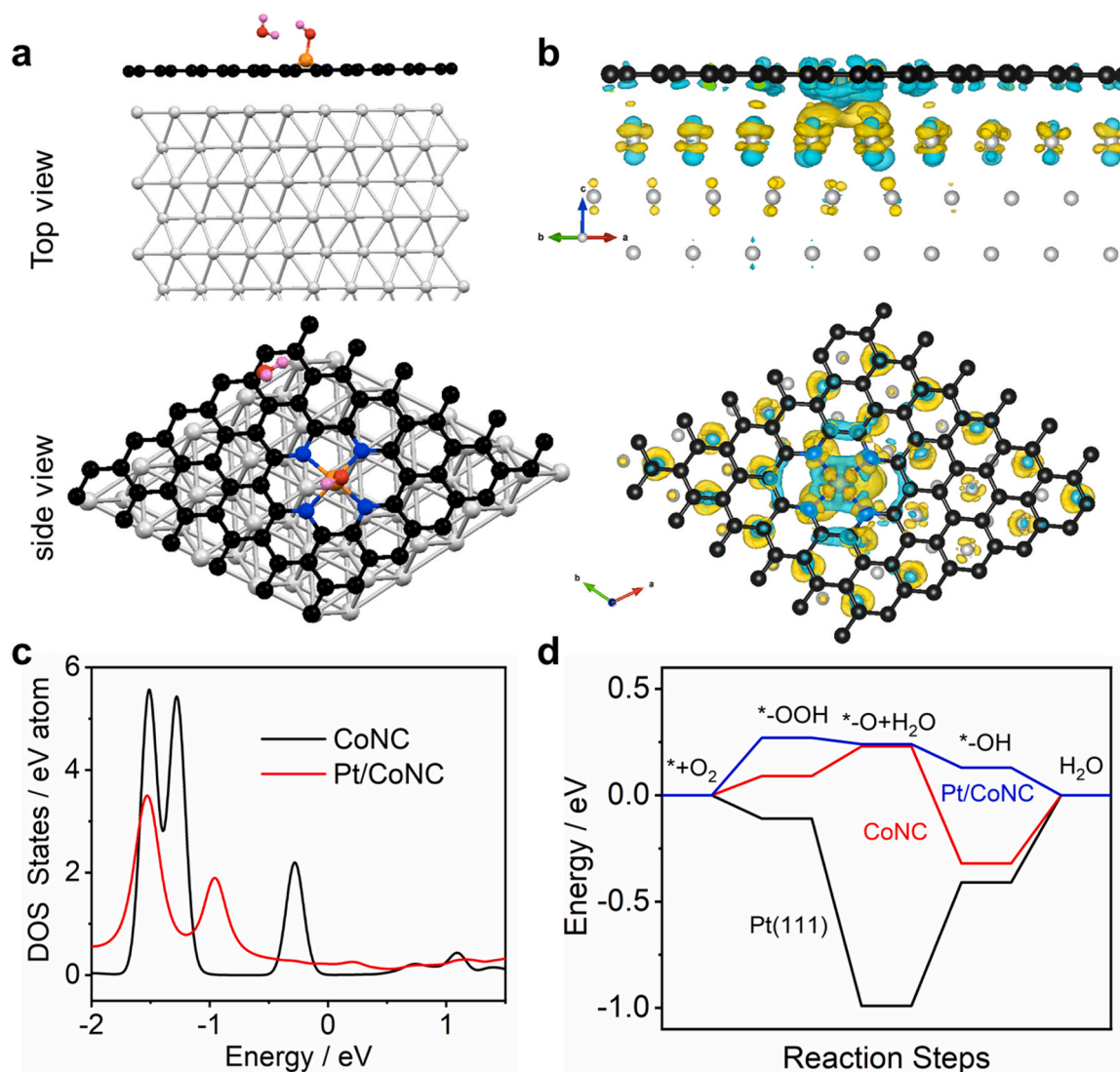
Fig. 9. (a) Optimized atomic structure of the fourth step of ORR at interface between Pt (111) surface and Co-NC layer. Pt-light grey, C-black, Co-orange, O-red, N-blue, H-pink. (b) The change of the charge density after formation of the interface between Co-NC and Pt (111) surface. Cyan and yellow "clouds" corresponding with decreasing and increasing of the charge density, respectively. (c) Partial densities of states of Co atoms in Co-NC and membrane with (red) and without (black) Pt substrate. Fermi energy set as zero. (d) Free energy diagram for four electrons ORR over Co-NC, Pt (111) substrate and Pt/Co-NC interface.

density of $Pt_3Co/CoNC$ and Pt/C was increased with the decreasing of the voltages. The discharge voltage of Pt/C was smaller than that of $Pt_3Co/CoNC$ as air electrode at the same current density, suggesting a better ORR activity of $Pt_3Co/CoNC$. The corresponding peak power density of the $Pt_3Co/CoNC$-based battery was 187 mW cm^{-2}, surpassing that of the Pt/C-based battery (83 mW cm^{-2}). Fig. 10c showed the constant current discharge over a series of current density at $2 - 40$ mA cm^{-2} to evaluate the rate performance. The $Pt_3Co/CoNC$ air electrode renders the voltages of 1.28, 1.25, 1.20, 1.12, 0.99 V at the current densities of 2, 5, 10, 20, 40 mA cm^{-2}, respectively, indicating excellent discharge rate performance of $Pt_3Co/CoNC$. When the current density was reduced to 2 mA cm^{-2}, the discharge recovered to 1.28 V, suggesting the super durability of $Pt_3Co/CoNC$ air electrode. Fig. 10d showed the depth discharge curves of the $Pt_3Co/CoNC$ and Pt/C catalysts at current densities of 5 mA cm^{-2}. The $Pt_3Co/CoNC$ exhibited a specific capacity of 768.9 mA h g^{-1} (normalized to the mass of the lost zinc) at a constant current density of 5 mA cm^{-2}, higher than that of Pt/C (622.5 mA h g^{-1}) as a comparison.

4. Conclusion

In summary, the metal-support coupling strategy was designed to enhancing the intrinsic activity of Pt by combining atomically ordered Pt_xM (M=Co, Zn) nanoparticles with the active Co/Zn-NC sites. The Co/Zn-NC sites could provide abundant surface structure to anchor the precursor of Pt and provide metal sources to formation the atomically ordered PtZn/ZnNC, PtCo/CoNC and $Pt_3Co/CoNC$ at high temperature. Compared with PtZn/ZnNC, PtCo/CoNC, the $Pt_3Co/CoNC$ exhibited uniformly distributed Pt_3Co nanoparticles and unique morphologies of Co/Zn-NC support (i.e., high surface areas, homogeneous polyhedron structure and electronic conductivity), resulting in the excellent catalytic activity and ideal stability towards ORR. The enhanced properties could be ascribed to the unique coupling effect between intermetallic Pt_3Co and Co-NC sites, which could regulate the electronic structure and weaken the activation energy to break O-O bonds. Furthermore, $Pt_3Co/CoNC$ displayed the peak power density of 187 mW cm^{-2} and discharge potential of 1.25 V at the current densities of 5 mA cm^{-2} when used as the air electrode in Zn-air battery. This work explores an innovative Co-NC supports to anchor Pt-based intermetallic compound and to regulate their intrinsic activity and stability based on metal-support coupling
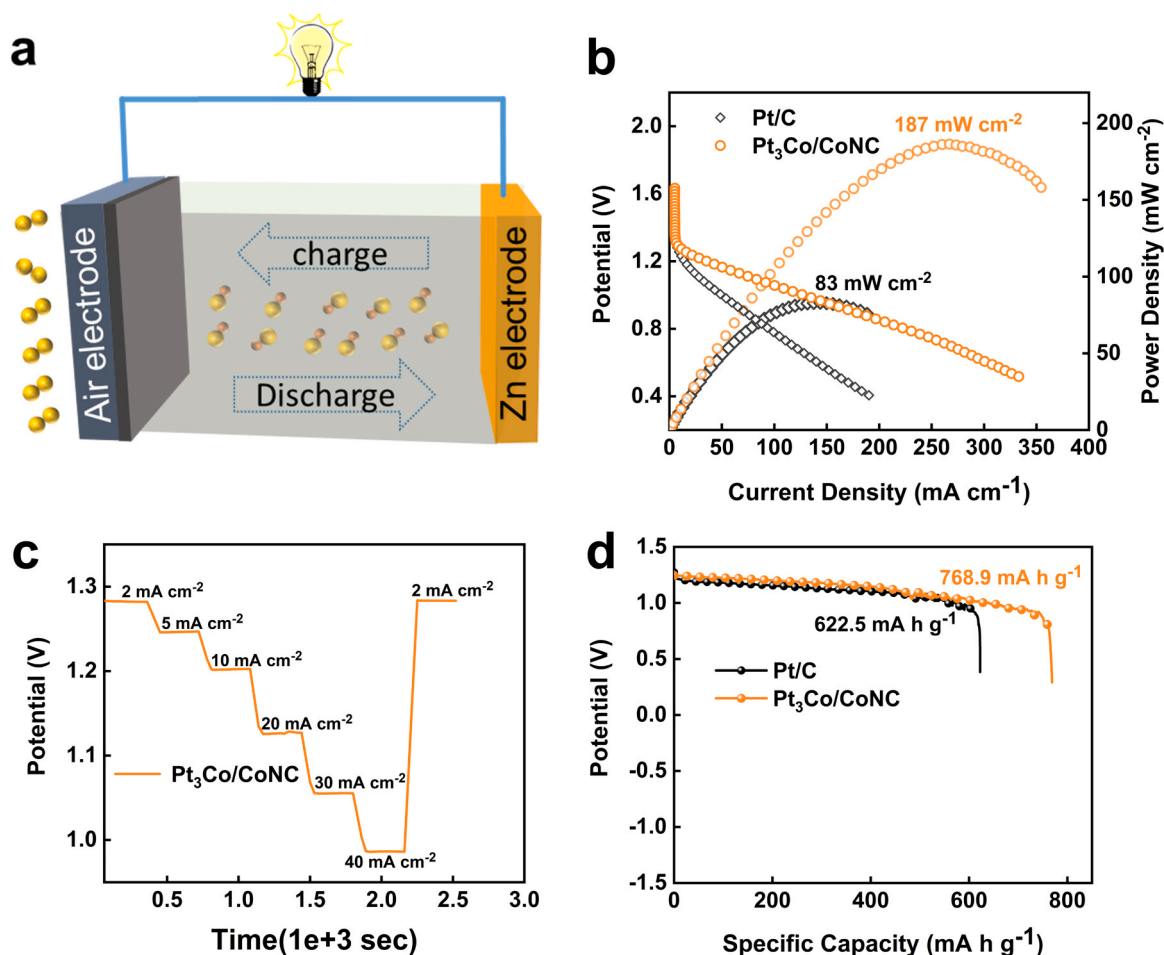
Fig. 10. (a) Schematic of the aqueous rechargeable Zn-air batteries (ZABs) using Pt$_3$Co/CoNC as the air cathode. (b) Discharge polarization curves of the Pt$_3$Co/CoNC and Pt/C air electrodes for the rechargeable ZABs and the corresponding power density curves. (c) Discharge curves of the Pt$_3$Co/CoNC at different current densities. (d) Discharge curves of the ZABs of Pt$_3$Co/CoNC and Pt/C catalysts at current densities of 5 mA cm^{-2}.

effects.

CRediT authorship contribution statement

Xiao Weiping: Writing – review & editing, Conceptualization, Supervision. **Yan Daqiang:** Data curation, Methodology, Visualization, Writing – original draft, Writing – review & editing. **Zhao Qin:** Data curation, Writing – original draft. **Bukhvalov Danil:** Software, Writing – original draft. **Yang Xiaofei:** Funding acquisition, Supervision, Writing – review & editing.

Declaration of Competing Interest

The authors declare that they have no known competing financial interests or personal relationships that could have appeared to influence the work reported in this paper.

Data Availability

The authors do not have permission to share data.

Acknowledgments

Appendix A. Supporting information

Supplementary data associated with this article can be found in the online version at doi:10.1016/j.apcatb.2024.123740.

References

[1] V. Beermann, M.E. Holtz, E. Padgett, J.F. de Araujo, D.A. Muller, P. Strasser, Real-time imaging of activation and degradation of carbon supported octahedral Pt–Ni alloy fuel cell catalysts at the nanoscale using in situ electrochemical liquid cell STEM, Energy Environ. Sci. 12 (2019) 2476–2485.

[2] S. Chen, J. Zhao, H. Su, H. Li, H. Wang, Z. Hu, J. Bao, J. Zeng, Pd-Pt tesseracts for the oxygen reduction reaction, J. Am. Chem. Soc. 143 (2021) 496–503.

[3] F. Armillotta, D. Bidoggia, S. Baronio, P. Biasin, A. Annese, M. Scardamaglia, S. Zhu, B. Bozzini, S. Modesti, M. Peressi, E. Vesselli, Single metal atom catalysts and ORR: H-bonding, solvation, and the elusive hydroperoxyl intermediate, ACS Catal. 12 (2022) 7950–7959.

[4] T. Wang, Y. Zhang, B. Huang, B. Cai, R.R. Rao, L. Giordano, S.-G. Sun, Y. Shao-Horn, Enhancing oxygen reduction electrocatalysis by tuning interfacial hydrogen bonds, Nat. Catal. 4 (2021) 753–762.

[5] W. Wan, Y. Zhao, S. Wei, C.A. Triana, J. Li, A. Arcifa, C.S. Allen, R. Cao, G. R. Patzke, Mechanistic insight into the active centers of single/dual-atom Ni/Fe-based oxygen electrocatalysts, Nat. Commun. 12 (2021) 5589.

[6] R. Gao, J. Wang, Z.-F. Huang, R. Zhang, W. Wang, L. Pan, J. Zhang, W. Zhu, X. Zhang, C. Shi, J. Lim, J.-J. Zou, Pt/Fe$_2$O$_3$ with Pt–Fe pair sites as a catalyst for oxygen reduction with ultralow Pt loading, Nat. Energy 6 (2021) 614–623.

[7] S. Kim, J. Kwag, C. Machello, S. Kang, J. Heo, C.F. Reboul, D. Kang, S. Kang, S. Shim, S.-J. Park, B.H. Kim, T. Hyeon, P. Ercius, H. Elmlund, J. Park, Correlating 3D surface atomic structure and catalytic activities of Pt nanocrystals, Nano Lett. 21 (2021) 1175–1183.

[8] J. Guan, S. Yang, T. Liu, Y. Yu, J. Niu, Z. Zhang, F. Wang, Intermetallic FePt@PtBi Core–Shell Nanoparticles for Oxygen Reduction Electrocatalysis, Angew. Chem. Int. Ed. 60 (2021) 21899–21904.

[9] Y.-F. Wu, J.-W. Ma, Y.-H. Huang, Enhancing oxygen reduction reaction of Pt–Co/C nanocatalysts via synergetic effect between Pt and Co prepared by one-pot synthesis, Rare Met. 42 (2023) 146–154.

[10] C. Yang, H.-B. Wang, P. Liang, B.-F. Wu, L. Zhao, P.-S. Leng, L. Lv, H.-Z. Wan, H. Wang, Size and structure tuning of FePt nanoparticles on hollow mesoporous carbon spheres as efficient catalysts for oxygen reduction reaction, Rare Met. 42 (2023) 1865–1876.

[11] M. Zhou, C. Li, J. Fang, Noble-metal based random alloy and intermetallic nanocrystals: syntheses and applications, Chem. Rev. 121 (2021) 736–795.

[12] S. Zaman, Y.Q. Su, C.L. Dong, R. Qi, L. Huang, Y. Qin, Y.C. Huang, F.M. Li, B. You, W. Guo, Q. Li, S. Ding, B. Yu Xia, Scalable molten salt synthesis of platinum alloys planted in metal-nitrogen-graphene for efficient oxygen reduction, Angew. Chem. Int. Ed. 61 (2022) e202115835.

[13] Q. Cheng, S. Yang, C. Fu, L. Zou, Z. Zou, Z. Zhang, H. Yang, High-loaded sub-6 nm Pt1Co1 intermetallic compounds with highly efficient performance expression in PEMFCs, Energy Environ. Sci. 15 (2022) 278–286.

[14] J. Liang, Z. Zhao, N. Li, X. Wang, S. Li, X. Liu, T. Wang, G. Lu, D. Wang, B. J. Hwang, Y. Huang, D. Su, Q. Li, Biaxial strains mediated oxygen reduction electrocatalysis on fenton reaction resistant L10-PtZn Fuel Cell Cathode, Adv. Energy Mater. 10 (2020) 2000179.

[15] Z. Wang, X. Yao, Y. Kang, L. Miao, D. Xia, L. Gan, Structurally ordered low-Pt intermetallic electrocatalysts toward durably high oxygen reduction reaction activity, Adv. Funct. Mater. 29 (2019) 1902987.

[16] H. Adabi, A. Shakouri, N. Ul Hassan, J.R. Varcoe, B. Zulevi, A. Serov, J. R. Regalbuto, W.E. Mustain, High-performing commercial Fe–N–C cathode electrocatalyst for anion-exchange membrane fuel cells, Nat. Energy 6 (2021) 834–843.

[17] Y.-X. Du, Y.-T. Zhou, M.-Z. Zhu, Co-based MOF derived metal catalysts: from nano-level to atom-level, Tungsten 5 (2023) 201–216.

[18] Y. Jiang, Y.P. Deng, R. Liang, N. Chen, G. King, A. Yu, Z. Chen, Linker-compensated metal-organic framework with electron delocalized metal sites for bifunctional oxygen electrocatalysis, J. Am. Chem. Soc. 144 (2022) 4783–4791.

[19] W. Cheng, X. Zhao, H. Su, F. Tang, W. Che, H. Zhang, Q. Liu, Lattice-strained metal-organic-framework arrays for bifunctional oxygen electrocatalysis, Nat. Energy 4 (2019) 115–122.

[20] X. Ao, W. Zhang, B. Zhao, Y. Ding, G. Nam, L. Soule, A. Abdelhafiz, C. Wang, M. Liu, Atomically dispersed Fe-N-C decorated with Pt-alloy core-shell nanoparticles for improved activity and durability towards oxygen reduction, Energy Environ. Sci. 13 (2020) 3032–3040.

[21] Z. Cui, G. Fu, Y. Li, J.B. Goodenough, Ni3FeN-Supported Fe3Pt intermetallic nanoalloy as a high-performance bifunctional catalyst for metal-air batteries, Angew. Chem. Int. Ed. 56 (2017) 9901–9905.

[22] J.O. Ighalo, S. Rangabhashiyam, C.A. Adeyanju, S. Ogunniyi, A.G. Adeniyi, C. A. Igwegbe, Zeolitic imidazolate frameworks (ZIFs) for aqueous phase adsorption – a review, J. Ind. Eng. Chem. 105 (2022) 34–48.

[23] X. Han, Q. Wang, Z. Zheng, Z. Nan, X. Zhang, Z. Song, M. Ma, J. Zheng, Q. Kuang, L. Zheng, Size-controlled intermetallic PtZn nanoparticles on N-doped carbon support for enhanced electrocatalytic oxygen reduction, ACS Sustain. Chem. Eng. 9 (2021) 3821–3827.

[24] J. Chen, G. Qian, B. Chu, Z. Jiang, K. Tan, L. Luo, B. Li, S. Yin, Tuning d-band center of Pt by PtCo-PtSn heterostructure for enhanced oxygen reduction reaction performance, Small 18 (2022) 2106773.

[25] M.S. José, A. Emilio, D.G. Julian, G. Alberto, J. Javier, O. Pablo, S.-P. Daniel, The SIESTA method for ab initio order-N materials simulation, J. Phys.: Condens. Mat. 14 (2002) 2745.

[26] J.P. Perdew, K. Burke, M. Ernzerhof, Generalized gradient approximation made simple, Phys. Rev. Lett. 77 (1996) 3865–3868.

[27] N. Troullier, J.L. Martins, Efficient pseudopotentials for plane-wave calculations, Phys. Rev. B 43 (1991) 1993–2006.

[28] M. Loloei, S. Kaliaguine, D. Rodrigue, CO2-Selective mixed matrix membranes of bimetallic Zn/Co-ZIF vs. ZIF-8 and ZIF-67, Sep. Purif. Technol. 296 (2022) 121391.

[29] K. Zhou, B. Mousavi, Z. Luo, S. Phatanasri, S. Chaemchuen, F. Verpoort, characterization and properties of Zn/Co zeolitic imidazolate frameworks vs. ZIF-8 and ZIF-67, J. Mater. Chem. A. 5 (2017) 952–957.

[30] C. Zhan, H. Sun, L. Lü, L. Bu, L. Li, Y. Liu, T. Yang, W. Liu, X. Huang, Zinc intercalated lattice expansion of ultrafine platinum-nickel oxygen reduction catalyst for PEMFC, Adv. Funct. Mater. 33 (2023) 2212442.

[31] Y. Fei, M. Liang, L. Yan, Y. Chen, H. Zou, Co/C@cellulose nanofiber aerogel derived from metal-organic frameworks for highly efficient electromagnetic interference shielding, Chem. Eng. J. 392 (2020) 124815.

[32] J. Wang, G. Wu, W. Wang, W. Xuan, J. Jiang, J. Wang, L. Li, W.-F. Lin, W. Ding, Z. Wei, A neural-network-like catalyst structure for the oxygen reduction reaction: carbon nanotube bridged hollow PtCo alloy nanoparticles in a MOF-like matrix for energy technologies, J. Mater. Chem. A 7 (2019) 19786–19792.

[33] X. Li, Y. He, S. Cheng, B. Li, Y. Zeng, Z. Xie, Q. Meng, L. Ma, K. Kisslinger, X. Tong, S. Hwang, S. Yao, C. Li, Z. Qiao, C. Shan, Y. Zhu, J. Xie, G. Wang, G. Wu, D. Su, Atomic structure evolution of Pt-Co binary catalysts: single metal sites versus intermetallic nanocrystals, Adv. Mater. 33 (2021) 2106371.

[34] W. Xu, X. Chen, J. Chen, H. Jia, Bimetal oxide CuO/Co3O4 derived from Cu ions partly-substituted framework of ZIF-67 for toluene catalytic oxidation, J. Hazard. Mater. 403 (2021) 123869.

[35] Y. Zhu, J. Peng, X. Zhu, L. Bu, Q. Shao, C.-W. Pao, Z. Hu, Y. Li, J. Wu, X. Huang, A large-scalable, surfactant-free, and ultrastable Ru-doped Pt3Co oxygen reduction catalyst, Nano Lett. 21 (2021) 6625–6632.

[36] J. Woo, J.S. Lim, J.H. Kim, S.H. Joo, Heteroatom-doped carbon-based oxygen reduction electrocatalysts with tailored four-electron and two-electron selectivity, Chem. Commun. 57 (2021) 7350–7361.

[37] L. Liang, H. Jin, H. Zhou, B. Liu, C. Hu, D. Chen, Z. Wang, Z. Hu, Y. Zhao, H.W. Li, D. He, S. Mu, Cobalt single atom site isolated Pt nanoparticles for efficient ORR and HER in acid media, Nano Energy 88 (2021) 106221.

[38] N. Bhuvanendran, S. Ravichandran, Q. Xu, T. Maiyalagan, H. Su, A quick guide to the assessment of key electrochemical performance indicators for the oxygen reduction reaction: a comprehensive review, Int. J. Hydrog. Energy 47 (2022) 7113–7138.

[39] T. Kumeda, L. Laverdure, K. Honkala, M.M. Melander, K. Sakaushi, Cations determine the mechanism and selectivity of alkaline oxygen reduction reaction on Pt(111), Angew. Chem. Int. Ed. 62 (2023) e202312841.

[40] Z. Wu, Y. Wang, D. Liu, B. Zhou, P. Yang, R. Liu, W. Xiao, T. Ma, J. Wang, L. Wang, Hexagonal defect-rich MnOx/RuO2 with abundant heterointerface to modulate electronic structure for acidic oxygen evolution reaction, Adv. Funct. Mater. 33 (2023) 2307010.

[41] A. Kulkarni, S. Siahrostami, A. Patel, J.K. Nørskov, Understanding catalytic activity trends in the oxygen reduction reaction, Chem. Rev. 118 (2018) 2302–2312.

[42] X. Yang, D. Xia, Y. Kang, H. Du, F. Kang, L. Gan, J. Li, Unveiling the axial hydroxyl ligand on FeN4C electrocatalysts and its impact on the pH-dependent oxygen reduction activities and poisoning kinetics, Adv. Sci. 7 (2020) 2000176.

[43] X. Ao, W. Zhang, B. Zhao, Y. Ding, G. Nam, L. Soule, A. Abdelhafiz, C. Wang, M. Liu, Atomically dispersed Fe–N–C decorated with Pt-alloy core–shell nanoparticles for improved activity and durability towards oxygen reduction, Energy Environ. Sci. 13 (2020) 3032–3040.